J. Fluid Mech. (1991), *vol.* 231, *pp.* 395–415
Printed in Great Britain

Mass transport in two-dimensional water waves

By MOHAMED ISKANDARANI AND PHILIP L.-F. LIU
Joseph Defrees Hydraulics Laboratory, School of Civil and Environmental Engineering, Cornell University, Ithaca, NY 14853, USA

(Received 31 July 1990 and in revised form 15 March 1991)

Mass transport in various kind of two-dimensional water waves is studied. The characteristics of the governing equations for the mass transport depend on the ratio of viscous lengthscale to the amplitude of the free-surface displacement. When this ratio is small, the nonlinearity is important and the mass transport flow acquires a boundary-layer character. Numerical schemes are developed to investigate mass transport in a partially reflected wave and above a hump in the seabed. When the mass transport is periodic in the horizontal direction, a spectral scheme based on a Fourier–Chebyshev expansion, is presented for the solution of the equations. For the case of a hump on the seabed, the flow domain is divided into three regions. Using the spectral scheme, the mass transport in the uniform-depth regions is calculated first, and the results are used to compute the steady flow in the inhomogeneous flow region which encloses the hump on the seabed.

1. Introduction

On free-surface gravity waves, fluid particles possess, aside from the to-and-fro time-dependent motion, a small steady drift often called mass transport velocity. The drift motion is the result of a non-zero mean momentum flux generated by the velocity fluctuations. The magnitude of the steady velocity is small compared to the primary oscillations; nevertheless, it is responsible for the migration of the fluid particles. The aim of this paper is to investigate the mass transport induced in two-dimensional water waves.

Several approximations are usually made to simplify the analysis of the steady flow (Longuet-Higgins 1953; Riley 1965; Stuart 1966; Dore 1976). First, the velocity is expanded in an asymptotic series in terms of a small parameter α,

$$\boldsymbol{v} = \alpha \boldsymbol{v}_1 + \alpha^2 \boldsymbol{v}_2 + \ldots, \quad \alpha = \bar{k}a \ll 1, \tag{1}$$

where a is the amplitude of the oscillation, and $\bar{k}$ is the wavenumber of the surface wave. Second, the first-order motion, $O(\alpha)$, is assumed to be periodic in time with zero mean:

$$\bar{\boldsymbol{v}}_1 = \frac{\sigma}{2\pi} \int_0^{\sigma/(2\pi)} \boldsymbol{v}_1(t)\, \mathrm{d}t = 0, \tag{2}$$

where the overbar denotes a time average over a period, and σ is the wave frequency. The steady flow is hence given, to a first approximation, by the time average of the second-order motion, $\bar{\boldsymbol{v}}_2$, which is often referred to as the steady streaming or Eulerian streaming (e.g. Batchelor 1967). The mass transport $\boldsymbol{v}_{\mathrm{m}}$, defined as the time average of the Lagrangian velocity, becomes (e.g. Longuet-Higgins 1953)

$$\boldsymbol{v}_{\mathrm{m}} = \bar{\boldsymbol{v}}_2 + \boldsymbol{v}_{\mathrm{s}} + O(\alpha^3), \boldsymbol{v}_{\mathrm{s}} = \overline{\int_{t_0}^{t} \boldsymbol{v}_1 \, \mathrm{d}t' \cdot \nabla \boldsymbol{v}_1}, \tag{3}$$

where $\boldsymbol{v}_s$ is the Stokes drift. Third, the $O(\alpha)$ motion is irrotational, $\nabla \times \boldsymbol{v}_1 = 0$, and can be described with a velocity potential. This assumption is not valid near the flow boundaries where shear layers develop to accommodate either the no-slip condition on the seabed, or the continuity of shear stress at the free surface. The shear layers, also called Stokes' boundary layers, have a small thickness $\epsilon = O(\bar{k}(\nu/\sigma)^{\frac{1}{2}})$, where ν is the kinematic viscosity.

Dore (1976) gives a derivation of the three-dimensional equations governing mass transport in the fluid core, i.e. 'far' from the Stokes boundary layers. These equations describe the transport of the $O(\alpha^2)$ mean vorticity by convection, vortex stretching, and viscous diffusion. The interplay between diffusion and convection/vortex stretching is determined by the ratio $\delta = \epsilon/\alpha$ of the viscous lengthscale to the amplitude of the oscillatory motion. When δ is large, viscous diffusion dominates, and the vorticity is expected to diffuse in the whole domain. When δ is sufficiently small, convection and vortex stretching are expected to be the predominant mode of transport in the core of the fluid. However, next to the boundaries, large normal gradients of the vorticity develop to balance the governing equations and compensate for the smallness of δ. The question hence arises whether convection would prevent the mean vorticity from spreading into the whole region. The steady streaming would then remain confined within an outer boundary layer, of thickness δ, often referred to as the Stuart layer. The double boundary layer would be much larger than the Stokes' boundary layer ($\epsilon \ll \delta$), but smaller than the typical dimension of the problem ($\delta \ll 1$). Based on the boundary-layer approximation, Stuart (1966) and Riley (1965) obtained analytical solutions, in the form of asymptotic series, for the Stuart layer generated by an oscillating cylinder in an infinite fluid region. Outside the Stuart layer, the vorticity was assumed to be zero and the steady streaming also vanished.

The experiments of Bertelsen, Svardal & Tjøtta (1973) on the steady streaming induced by an oscillating cylinder confirmed the existence of the Stuart boundary layer. The measurements compared well with Riley's solution within a distance δ from the surface of the inner cylinder. Farther away, the experimental results gave a stronger velocity than predicted by the series solution. The numerical experiments of Duck & Smith (1979) proved that the discrepancies were due to the finite flow region in the experiment. Moreover, the work of Batchelor (1967) shows that in the limit $\delta \to 0$, a steady flow with closed streamlines becomes essentially inviscid but rotational away from the boundaries, and the vorticity distribution becomes more or less uniform in the core region. In the context of water waves, Haddon & Riley (1983) performed a number of numerical simulations for mass transport in standing waves, and their results support the conclusions of Duck & Smith (1979).

The aim of this work is to investigate mass transport for a broad range of the parameter δ, and for different physical situations. To this end, various numerical models, that do not inherently restrict the value of δ, are developed to solve the governing equations. The first physical situation considered consists of a spatially periodic wave in water of constant depth where the mean flow is also periodic. The prescription of lateral boundary conditions can be avoided if the dependent variables in the problem are expanded in a Fourier series. Section (3) elaborates on the spectral solution of the periodic mass transport. The numerical model is then used to compute the mass transport in partially reflected waves, for a range of reflection coefficients, and for different values of δ.

The second situation concerns the mass transport in waves travelling over a variable topography, where the bathymetrical features are large enough to affect the

wave motion. The example consists of a symmetrical hump located on constant water depth. The computational domain is truncated and adequate boundary conditions are applied at the lateral sides. The first-order motion is spatially aperiodic over the variable bathymetry, and the representation of the mass transport with Fourier functions loses its advantages. A finite-element scheme is chosen for the numerical solution to resolve the irregular geometry of the bathymetry. The solution shows the formation of a circulation cell downstream of the disturbance whose size depends on the parameter δ and height of the hump.

2. Governing equations

Dore (1976) derived the three-dimensional equations governing mass transport in the core region; the two-dimensional stream function–vorticity formulation of those equations is

$$\left(u_s+\frac{\partial\bar{\psi}_2}{\partial y}\right)\frac{\partial\bar{\omega}_2}{\partial x}+\left(v_s-\frac{\partial\bar{\psi}_2}{\partial x}\right)\frac{\partial\bar{\omega}_2}{\partial y}=\delta^2\nabla^2\bar{\omega}_2, \tag{4}$$

where $\bar{\psi}_2$ and $\bar{\omega}_2$ are the stream function and vorticity associated with the $O(\alpha^2)$ steady motion, and where the following dimensionless variables have been used:

$$x=\bar{k}x', \quad t=\sigma t', \quad v=(\bar{k}/\sigma)\,v', \quad \omega=\omega'/\sigma, \quad \psi=(\bar{k}^2/\sigma)\,\psi'.$$

The components of the Eulerian streaming, $\bar{u}_2$ and $\bar{v}_2$, are derived from the stream function as follows

$$\bar{u}_2=\frac{\partial\bar{\psi}_2}{\partial y}, \quad \bar{v}_2=-\frac{\partial\bar{\psi}_2}{\partial x}. \tag{5}$$

Moreover, the vorticity and the stream function obey the compatibility equation

$$\nabla^2\bar{\psi}_2+\bar{\omega}_2=0. \tag{6}$$

We also define a Lagrangian stream function, χ, such that the mass transport velocity components (u_m, v_m) bear the same relation to χ as $(\bar{u}_2, \bar{v}_2)$ to $\bar{\psi}_2$. The Lagrangian and Eulerian stream functions χ and $\bar{\psi}_2$ are related via

$$\chi=\bar{\psi}_2+\overline{\int\frac{\partial\psi_1}{\partial y}\,dt\,\frac{\partial\psi_1}{\partial x}}, \tag{7}$$

where ψ_1 refers to the stream function of the first-order oscillatory flow.

As indicated earlier, (4) is not valid near the seabed and free surface because the $O(\alpha)$ motion is not irrotational. The analysis of the steady flow in these neighbourhoods is necessary to derive boundary conditions for (4) and (6). Longuet-Higgins (1953) invoked the boundary-layer approximation to study the flow next to a solid boundary, or next to a free surface. At $O(\alpha)$, the vorticity generated is harmonic in time and remains confined to the shear layers of thickness $O(\epsilon \ll 1)$. However, the products of the leading velocity components produce a steady Reynolds stress at $O(\alpha^2)$. The gradient of the steady Reynolds stress generates an Eulerian steady streaming inside the boundary layer adjacent to the seabed and a steady vorticity in the free-surface boundary layer. Measurements of the steady streaming at the seabed and the steady vorticity at the surface can be found in Russell & Osorio (1958) and Longuet-Higgins (1960). Both the steady streaming and the steady vorticity are of $O(\alpha^2)$ and persist outside the Stokes' layer to form a driving mechanism for the mass transport in the core of the fluid region.

If the first-order potential velocity is given by $\mathrm{Re}[(U, V)\,\mathrm{e}^{-\mathrm{i}t}]$, Longuet-Higgins (1953) gives the following expression for the Eulerian streaming tangential to the boundary and at the outer edge of the Stokes' layer:

$$(\bar{u}_2)_s = \mathrm{Re}\left[\frac{3\mathrm{i}-3}{4} U^s \frac{\partial U^{s*}}{\partial s}\right], \tag{8}$$

where U^s is the tangential potential velocity of the fluid at the solid surface, s is the arclength along the boundary, an asterisk denotes the complex conjugate, and Re indicates the real part of a complex quantity. Longuet-Higgins' expression for the mean vorticity at the edge of the free-surface boundary layer is

$$\bar{\omega}_2 = \mathrm{Re}\left[2\mathrm{i} \frac{\partial U^s}{\partial s} \frac{\partial U^{n*}}{\partial s}\right], \tag{9}$$

where $\partial U^s/\partial s$ and $\partial U^{n*}/\partial s$ are the tangential gradients of the tangential and normal potential velocity of the fluid evaluated on the free surface.

The velocity component normal to the seabed can be computed from the continuity equations and shown to be of $O(\epsilon\alpha^2)$. The seabed is hence a streamline in the Eulerian and Lagrangian sense:

$$\bar{\psi}_2 = \chi = 0. \tag{10}$$

Also, the free surface is a Lagrangian streamline, i.e.

$$\chi = \text{constant}. \tag{11}$$

The choice of the constant is at our disposal. Its value determines the total amount of flux at any vertical section. An obvious choice is to equate the stream function at the seabed and free surface so that the net drift at any section is zero. This is a reasonable assumption in a closed system where the establishment of a recirculation pattern, in the absence of sources and sinks, is imperative to satisfy the conservation of mass. The specification of a net flux amounts to a condition on the mean $O(\alpha^2)$ pressure gradient (Ünlüata & Mei 1970). In all cases considered here the system has been regarded as closed, and the net mass flux is required to vanish.

In the following sections, we compute the mass transport by solving (4) and (6) subject to (8)–(11). The overbar and the subscript 2 on all second-order mean quantities will be dropped, and capital letters will be used to refer to first-order potential flow quantities.

3. Partially reflected waves

When the water depth is a constant h, the $O(\alpha)$ free-surface displacement, for small-amplitude partially reflected waves with a reflection coefficient R, is given by the real part of

$$\zeta = (\mathrm{e}^{\mathrm{i}kx} + R\,\mathrm{e}^{-\mathrm{i}kx})\,\mathrm{e}^{-\mathrm{i}t}. \tag{12}$$

The x- and y-axes are horizontal and vertical respectively with the origin located at the still water level. The wave is purely progressive in the positive x-direction when $R = 0$, and purely standing for $R = 1$. The x and y potential velocity components, corresponding to the free surface displacement in (12), are

$$U = \frac{k}{\beta} \frac{\cosh k(y+h)}{\cosh kh} (\mathrm{e}^{\mathrm{i}kx} - R\,\mathrm{e}^{-\mathrm{i}kx}),$$

$$V = \frac{-\mathrm{i}k}{\beta} \frac{\sinh k(y+h)}{\cosh kh} (\mathrm{e}^{\mathrm{i}kx} + R\,\mathrm{e}^{-\mathrm{i}kx}),$$

where $\beta = \sigma^2/(\bar{k}g) = k\tanh kh$. The Stokes drift can be written analytically:

$$u_s(x,y) = \frac{k^3\cosh 2k(y+h)}{2\beta^2\cosh^2 kh}(1-RR^*), \quad v_s(x,y) = 0 \tag{13}$$

and has no vertical component. For the second-order mean motion, the seabed is a streamline whose value is arbitrarily set to zero:

$$\psi(x,-h) = \chi(x,-h) = 0. \tag{14}$$

The Eulerian streaming at the seabed (strictly speaking at the outer edge of the Stokes boundary layer) is (Longuet-Higgins 1953)

$$u(x,-h) = u^b(x) = \frac{3k^3}{4\beta^2\cosh^2 kh}[-\mathrm{i}R\,\mathrm{e}^{-\mathrm{i}2kx} + (1-RR^*) + \mathrm{i}R^*\,\mathrm{e}^{\mathrm{i}2kx}]. \tag{15}$$

The Lagrangian stream function is set to zero at the free surface, i.e.

$$\psi(x,0) = \psi^s = -\frac{k^2\sinh 2kh}{4\beta^2\cosh^2 kh}(1-RR^*) \tag{16}$$

and the vorticity is given by

$$\omega(x,0) = \omega^s = \frac{-k^4\sinh 2kh}{\beta^2\cosh^2 kh}(1-RR^*). \tag{17}$$

From (13)–(17), the mass transport has to be periodic in the direction of wave propagation because of the periodic forcing terms.

The present numerical scheme rests on a spectral representation of the dependent variables ψ and ω. The shape functions in the horizontal direction are Fourier functions that guarantee the periodicity of the flow in the x-direction, and allow the no-slip condition on the velocity to be transformed analytically into an integral constraint on the vorticity. The shape functions in the vertical direction are Chebyshev polynomials that allow aperiodic boundary conditions to be prescribed at the free surface and the seabed. Moreover, among the many properties of Chebyshev polynomials (Boyd 1989), is the ability to sum Chebyshev series efficiently using fast Fourier transforms (FFT); these sums arise when the nonlinear convection term in (4) is evaluated. The method of 'false transients' (Roache 1982) is used to control the development of the nonlinearities: a time-dependent term is introduced in (4), and the coefficients of the Fourier–Chebyshev expansions are made dependent on the fictitious time t. When the spectral series for the stream function and vorticity are substituted in the governing equations (4) and (6), and a Tau procedure (Canuto *et al.* 1988) invoked, a system of ODE's (in time t) is obtained. The time integration is performed with finite differences, and the solution is advanced in time until a steady state is reached. The details of this numerical formulation are presented next. References on spectral methods and their applications can be found in Gottlieb & Orszag (1977) and Canuto *et al.* (1988).

3.1. *Spectral scheme*

Since the equations have spatial periodicity and the Chebyshev polynomials are defined over the interval $[-1,1]$, we define the new variables $\xi = 2kx$ and $\eta = (2/h)y+1$. Let

$$\begin{pmatrix}\omega\\ \psi\end{pmatrix} = \sum_{n=-N}^{N}\sum_{m=0}^{M} T_m(\eta)\,\mathrm{e}^{\mathrm{i}n\xi}\begin{pmatrix}\Omega_{m,n}\\ \Psi_{m,n}\end{pmatrix}, \quad \begin{pmatrix}\Omega_{m,-n}\\ \Psi_{m,-n}\end{pmatrix} = \begin{pmatrix}\Omega^*_{m,n}\\ \Psi^*_{m,n}\end{pmatrix}, \tag{18}$$

where $T_m(\eta)$ is the Chebyshev polynomial of the first kind and order m (Canuto *et al.* 1988).

The series expansions are substituted in the transient form of (4) and in (6), and the Chebyshev–Tau method is applied to the resultant equations to obtain

$$\frac{\mathrm{d}\Omega_{m,n}}{\mathrm{d}t}-\frac{4\delta^2}{h^2}\left[\sum_{p=m+2,2}^{M}\left(\frac{p(p^2-m^2)}{c_m}\Omega_{p,n}\right)-(nkh)^2\Omega_{m,n}\right]-R_{m,n}=0, \tag{19}$$

$$\sum_{p=m+2,2}^{M}\left(\frac{p(p^2-m^2)}{c_m}\Psi_{p,n}\right)-(nkh)^2\Psi_{m,n}+\tfrac{1}{4}h^2\Omega_{m,n}=0 \tag{20}$$

for $m=0,1,\ldots,M-1$, and $n=0,1,\ldots,N$. The 2 in the subscript of the summation sign indicates the increments of the index p; $c_0=2$ for $m=0$ and $c_m=1$ for $m\geqslant 1$. The $R_{m,n}$ are the Fourier–Chebyshev coefficients of the nonlinear convection term

$$\sum_{m=0}^{M}\sum_{n=-N}^{N}R_{m,n}T_m(\eta)\,\mathrm{e}^{\mathrm{i}n\xi}=\frac{4k}{h}\left[\left(\frac{\partial\psi}{\partial\xi}-\frac{1}{2k}v_{\mathrm{s}}\right)\frac{\partial\omega}{\partial\eta}-\left(\frac{\partial\psi}{\partial\eta}+\frac{h}{2}u_{\mathrm{s}}\right)\frac{\partial\omega}{\partial\xi}\right]. \tag{21}$$

The Fourier decomposition of the boundary conditions gives the following expressions:

$$\sum_{m=0}^{M}(-1)^m m^2\Psi_{m,n}=\tfrac{1}{2}hu_n^{\mathrm{b}},\quad \sum_{m=0}^{M}\Omega_{m,n}=\Omega_n^{\mathrm{s}}\quad (0\leqslant n\leqslant N), \tag{22a, b}$$

$$\sum_{m=0}^{M}(-1)^m\Psi_{m,n}=0,\quad \sum_{m=0}^{M}\psi_{m,n}=\Psi_n^{\mathrm{s}}\quad (0\leqslant n\leqslant N), \tag{23a, b}$$

where Ψ_n^{s}, Ω_n^{s} and u_n^{b} are the Fourier coefficients of ψ^{s}, ω^{s} and u^{b}:

$$\begin{pmatrix}\psi^{\mathrm{s}}\\ \omega^{\mathrm{s}}\\ u^{\mathrm{b}}\end{pmatrix}=\sum_{n=-N}^{N}\cdot\,\mathrm{e}^{\mathrm{i}n\xi}\begin{pmatrix}\Psi_n^{\mathrm{s}}\\ \Omega_n^{\mathrm{s}}\\ u_n^{\mathrm{b}}\end{pmatrix} \tag{24}$$

When finite differences are used for the time integration, (19), (20), and (22)–(23) yield a system of $2(M+1)(N+1)$ nonlinear algebraic equations for the $2(M+1)(N+1)$ unknowns $\psi_{m,n}$ and $\Omega_{m,n}$. In order to linearize the problem, the convection term, $R_{m,n}$, in (19) is approximated with its value at the current time level. This approximation presents two main advantages. First, since $R_{m,n}$ in (19) is known, the no-slip condition (22*a*) becomes the only tie between the vorticity and stream function equations. If an adequate boundary condition for the vorticity is provided, one can solve (19) subject to (22) to update the vorticity field, and then (20) subject to (23) to find the corresponding stream function. Second, the different Fourier modes ($n=0,1,2,\ldots,N$) involved in (19) decouple, and the equations link only the $M+1$ Chebyshev modes of every Fourier mode. The same is true for (20) because it is linear. The nonlinear system of $2(N+1)(M+1)$ equations can thus be divided into two (one for $\Omega_{m,n}$ and another for $\Psi_{m,n}$) $(N+1)$ sets of $(M+1)$ linear equations. The computational cost, at each time step, to solve the set of linear systems is proportional to $(N+1)(M+1)^3$, as compared to $[(\mathrm{N}+1)(\mathrm{M}+1)]^3$ had the original system been solved directly. The trade-off comes in the number of steps required to converge to the steady-state solution, and in the overhead incurred when evaluating the convection term.

3.2. *Vorticity constraint*

The sequential solution of the vorticity and stream function equations hinges on the derivation of an appropriate no-slip boundary condition for the vorticity. To this end, the solution of the compatibility equation will be sought with the assumption of a periodic horizontal flow. The relation between the vertical derivative of the stream function and vorticity can then be stated explicitly. Let

$$\begin{pmatrix}\omega\\ \psi\end{pmatrix} = \sum_{n=-N}^{N} e^{in\xi}\begin{pmatrix}\Omega_n(\eta)\\ \Psi_n(\eta)\end{pmatrix} \tag{25}$$

and substitute in (6). The following differential equation and boundary condition are obtained for each Fourier mode $n = 0, 1, \ldots, N$:

$$\frac{d^2\Psi_n}{d\eta^2} - (nkh)^2\Psi_n + \tfrac{1}{4}h^2\Omega_n = 0, \tag{26}$$

$$\Psi_n(\eta = 1) = \Psi_n^s, \quad \Psi_n(\eta = -1) = 0. \tag{27}$$

The solution is given by

$$\Psi_0(\eta) = \tfrac{1}{2}\left[\Psi_0^s - \tfrac{1}{4}h^2\int_{-1}^{1}\Omega_0(\zeta)(\zeta-1)\,d\zeta\right](\eta+1) + \tfrac{1}{4}h^2\int_{-1}^{\eta}\Omega_0(\zeta)(\zeta-\eta)\,d\zeta \tag{28}$$

for $n = 0$, and

$$\Psi_n(\eta) = \left[\Psi_n^s - \frac{h}{4nk}\int_{-1}^{1}\Omega_n(\zeta)\sinh nkh(\zeta-1)\,d\zeta\right]\frac{\sinh nkh(\eta+1)}{\sinh 2nkh} + \frac{h}{4nk}\int_{-1}^{\eta}\Omega_n(\zeta)\sinh nkh(\zeta-\eta)\,d\zeta \tag{29}$$

for $n = 1, 2, \ldots, N$. The derivative, with respect to η, of the above two expressions is evaluated on the seabed and equated to the right-hand side of (22*a*) to give the following relations:

$$\int_{-1}^{1}\Omega_0(\zeta)(\zeta-1)\,d\zeta = \frac{4}{h}\left[\frac{\Psi_0^s}{h} - u_0^b\right], \tag{30}$$

$$\int_{-1}^{1}\Omega_n(\zeta)\frac{\sinh nkh(\zeta-1)}{\sinh 2nkh}\,d\zeta = \frac{2}{h}\left[\frac{2nk\Psi_n^s}{\sinh 2nkh} - u_n^b\right]. \tag{31}$$

The no-slip condition on the velocity has thus been recast into an integral condition on each Fourier mode of the vorticity. The final form of this boundary condition is obtained when the Fourier coefficients Ω_n in (30) and (31) are replaced by their Chebyshev series, $\Omega_n = \sum_{m=0}^{M}\Omega_{m,n}T_m(\eta)$. Thus

$$\sum_{m=0}^{M} S_{m,0}\Omega_{m,0} = \frac{4}{h}\left[\frac{\Psi_0^s}{h} - u_0^b\right], \quad S_{m,0} = \int_{-1}^{1}T_m(\eta)(\eta-1)\,d\eta, \tag{32}$$

$$\sum_{m=0}^{M} S_{m,n}\Omega_{m,n} = \frac{2}{h}\left[\frac{2nk\Psi_n^s}{\sinh 2nkh} - u_n^b\right], \quad S_{m,n} = \int_{-1}^{1}T_m(\eta)\frac{\sinh nkh(\eta-1)}{\sinh 2nkh}\,d\eta. \tag{33}$$

The expressions for the $S_{m,n}$ are given in the Appendix.

In the time integration, the viscous term in (19) is handled implicitly for the sake of numerical stability, while the nonlinear term is evaluated explicitly with a fourth-

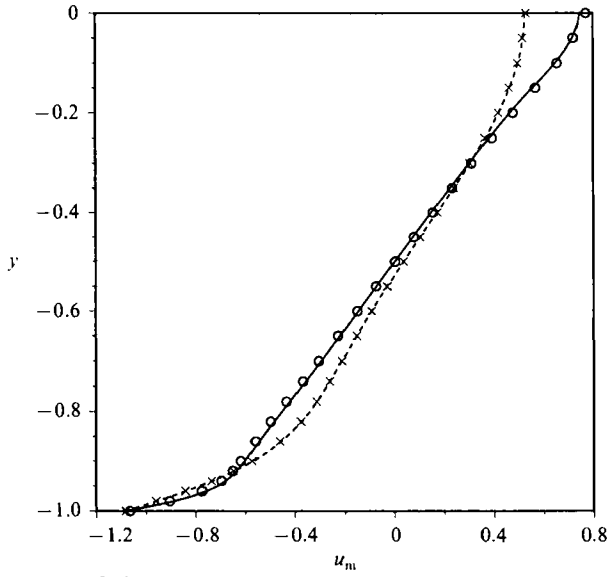

FIGURE 1. Comparison of the mass transport velocity profile under a standing wave at $x = \frac{1}{4}\pi$, midway between the node and antinode, as obtained from the spectral scheme (—, $\delta = 0.04$; – – –, $\delta = 0.1$) and the FEM scheme (○, $\delta = 0.04$; ×, $\delta = 0.1$).

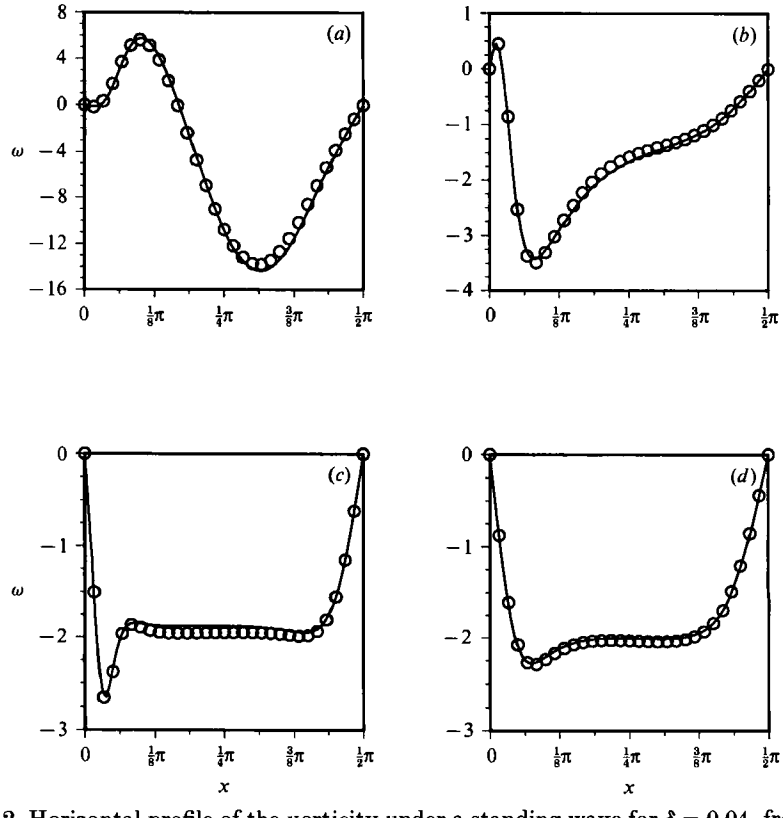

FIGURE 2. Horizontal profile of the vorticity under a standing wave for $\delta = 0.04$, from the spectral scheme(—), and FEM scheme (○) at (*a*) $y = -1.0$ (seabed), (*b*) $y = -0.9$, (*c*) $y = -0.6$, (*d*) $y = -0.2$.

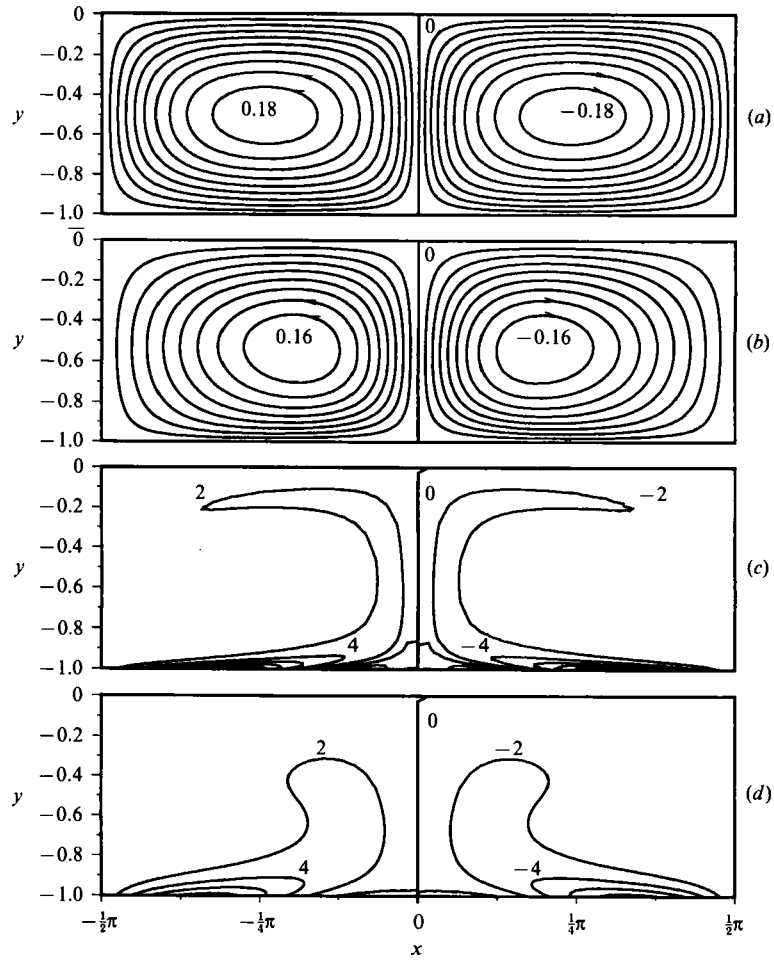

FIGURE 3. Lagrangian streamlines (*a*, *b*) and vorticity (*c*, *d*) contours for a standing wave $R = 1.0$: (*a*) $\delta = 0.04$, $\Delta\chi = 0.02$; (*b*) $\delta = 0.04$, $\Delta\omega = 2.0$; (*c*) $\delta = 0.10$, $\Delta\chi = 0.02$; (*d*) $\delta = 0.10$, $\Delta\omega = 2.0$.

order Runge–Kutta scheme. The time discretization of (19) yields the following algebraic equations:

$$\left[1-\frac{4\delta^2\Delta t}{h^2}(nkh)^2\right]\Omega_{m,n}^{t+\Delta t}-\frac{4\delta^2\Delta t}{h^2}\Omega_{m,n}^{(2),t+\Delta t}=\Omega_{m,n}^{t}+\Delta t R_{m,n}^{t}, \tag{34}$$

where $R_{m,n}^{t}$ is the convection term at time level t. The solution procedure is the following: (i) given the vorticity coefficients $\Omega_{m,n}^{t}$ at time t, the corresponding stream function coefficients $\Psi_{m,n}^{t}$ are obtained from (20) and (23); (ii) an estimate of the nonlinear term $R_{m,n}^{t}$ is calculated according to a Runge–Kutta 4 scheme; (iii) (34), (22*b*) and (32) or (33), are solved for the new vorticity coefficients $\Omega_{m,n}^{t+\Delta t}$; (iv) Steps (i)–(iii) are repeated until

$$|\Omega_{m,n}^{t+\Delta t}-\Omega_{m,n}^{t}|<10^{-5}.$$

3.3. *Numerical results*

The numerical simulations were performed by keeping the dimensionless wavenumber k and water depth h equal to 1 while the reflection coefficient, $|R|$, was varied from 0.1 to 1.0 in increments of 0.1. The standing-wave case ($|R| = 1$) is special

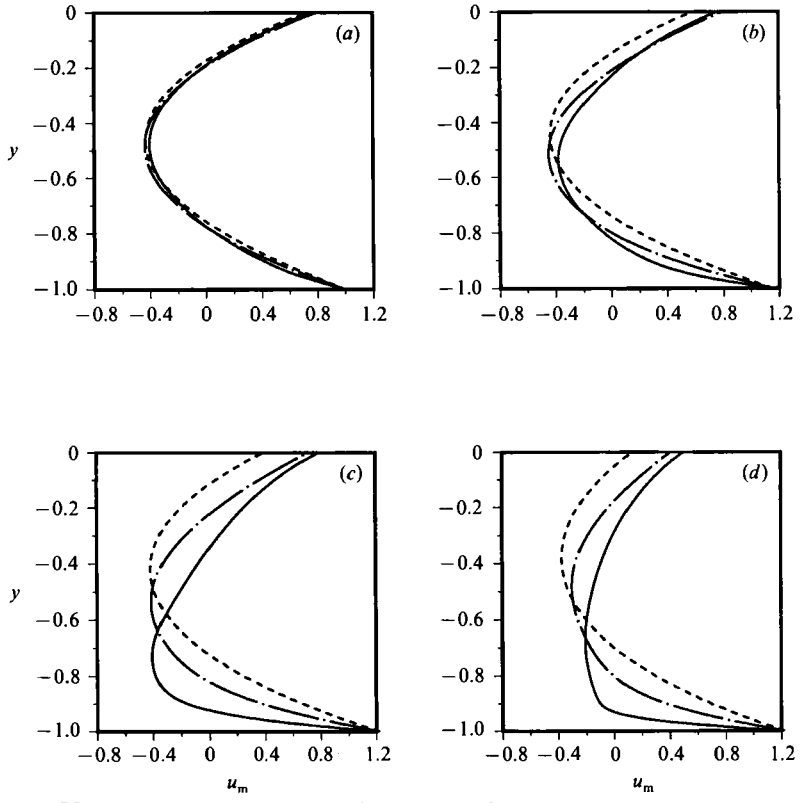

FIGURE 4. Mass transport velocity profile at $x = -\frac{1}{4}\pi$ for δ equal to 0.04 (—), 0.1 (—·—) and 100 (– –); (*a*) $R = 0.1$, (*b*) $R = 0.3$, (*c*) $R = 0.5$, (*d*) $R = 0.7$.

in that all forcing terms vanish ($\psi^s = \omega^s = u_s = 0$) except for the Eulerian streaming at the seabed. The latter becomes proportional to $\sin 2x$ and possesses symmetry about the nodal ($x = n\pi, n = 0, 1, \ldots$) and antinodal ($x = \frac{1}{2}(2n+1)\pi$) lines of the free surface; one can then deduce that $\psi = \omega = 0$ at these symmetry lines. The lateral sides are hence Dirichlet boundaries, and the mass transport equations can be solved by using the finite-element method (FEM) (see Baker 1983) within a finite domain between a node and an antinode (e.g. $0 \leqslant x \leqslant \frac{1}{2}\pi$). Figure 1 shows the mass transport profile at $x = \frac{1}{4}\pi$ (midway between the node and the antinode) as computed by FEM versus the spectral solution. The agreement is very good for the two δ-values considered, 0.1 and 0.04, and the comparison provides confidence in both numerical schemes. The formation of the Stuart boundary layer for small values of δ is evident in the large velocity gradients near $y \approx -h + O(\delta)$. Figure 2 (*a–d*) depicts the vorticity at different elevations for $\delta = 0.04$. The FEM and spectral solutions show some discrepancies near the seabed ($y = -1$), but the agreement is still good. The figures also show the uniform vorticity distribution inside the recirculation region, away from the lateral sides $x = 0, \frac{1}{2}\pi$, the seabed ($y = -1$), and the free surface ($y = 0$). Similar results were obtained in the numerical experiments of Haddon & Riley (1983). The streamlines are shown in figure 3 (*a*, *b*) where the formation of two cells is evident; the left and right cells rotate in the counterclockwise and clockwise direction respectively. The seabed boundary layers in each cell collide at $x = n\pi$ ($n = 0, 1, \ldots$), and deflect upward to form a vertical jet under the antinodes of the free surface. This jet remains attached to the symmetry line and shoots up until it

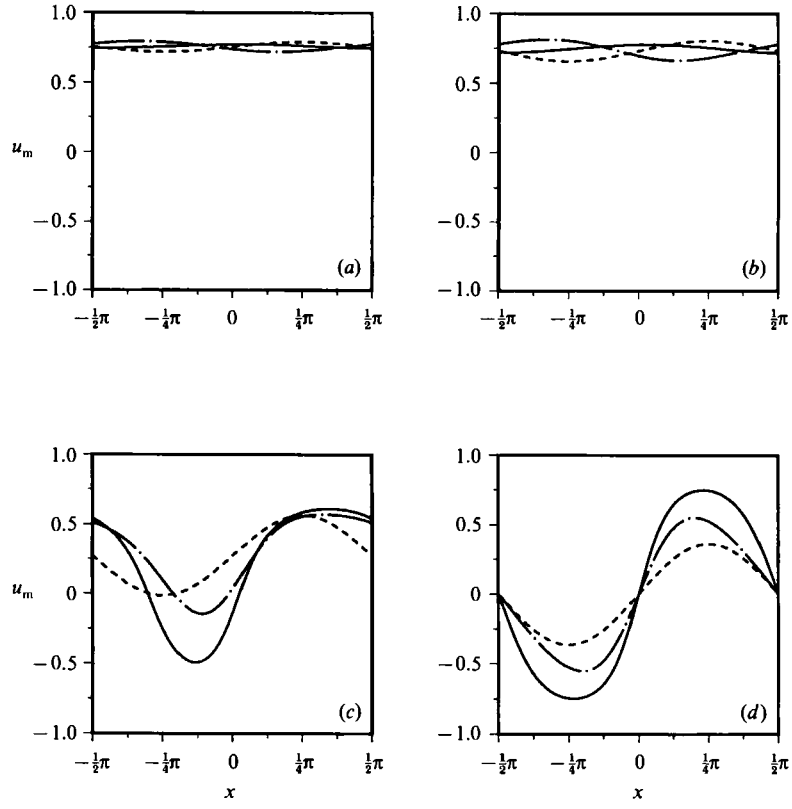

FIGURE 5. Mass transport velocity at free surface $y = 0$ for δ equal to 0.04 (—), 0.1 (—·—) and 100 (– –); (*a*) $R = 0.1$, (*b*) $R = 0.2$, (*c*) $R = 0.8$, (*d*) $R = 1.0$.

reaches the free surface. At this point, the flow becomes horizontal and starts forming the recirculating region that feeds fluid into the bottom boundary layer. Decreasing the parameter δ seems to confine a bigger part of the flow to the boundary regions. A comparison of the contours in figures 3(*a*) and 3(*b*) shows a more symmetrical distribution of the streamlines, and larger velocities near the nodal lines $x = \pm\frac{1}{2}\pi$. The closer streamlines in the jet, with decreasing δ, indicate an increase in the vertical velocity. The vorticity contours for $\delta = 0.1$ are shown in figure 3(*c*, *d*). Strong vorticity and its gradients appear near the seabed and in the jet. In the central part of the flow, however, the vorticity is more or less uniform. This could have been inferred from Batchelor's (1967) theorem concerning steady-state flows with closed streamlines. The velocity in the central region is smaller than near the boundaries but has still appreciable magnitudes; the mass transport persists outside the Stuart layer.

The dependency of the mass transport velocity on δ diminishes as the reflection decreases. This is illustrated in the velocity profiles at $x = -\frac{1}{4}\pi$, figure (4*a–d*). The velocity profile remains close to the parabolic shape associated with a purely progressive wave when $|R|$ is small ($|R| \leqslant 0.3$). The graphs depict the formation of the seabed boundary layer as δ decreases and $|R|$ increases. The large velocity gradients within a distance $O(\delta)$ of the seabed reveal the presence of this outer boundary layer. These gradients decrease appreciably away from the seabed, and tend to increase in the neighbourhood of the free surface. Figure 5(*a–d*) describes the dependency of the mass transport velocity at the free surface on the parameter δ; the influence increases

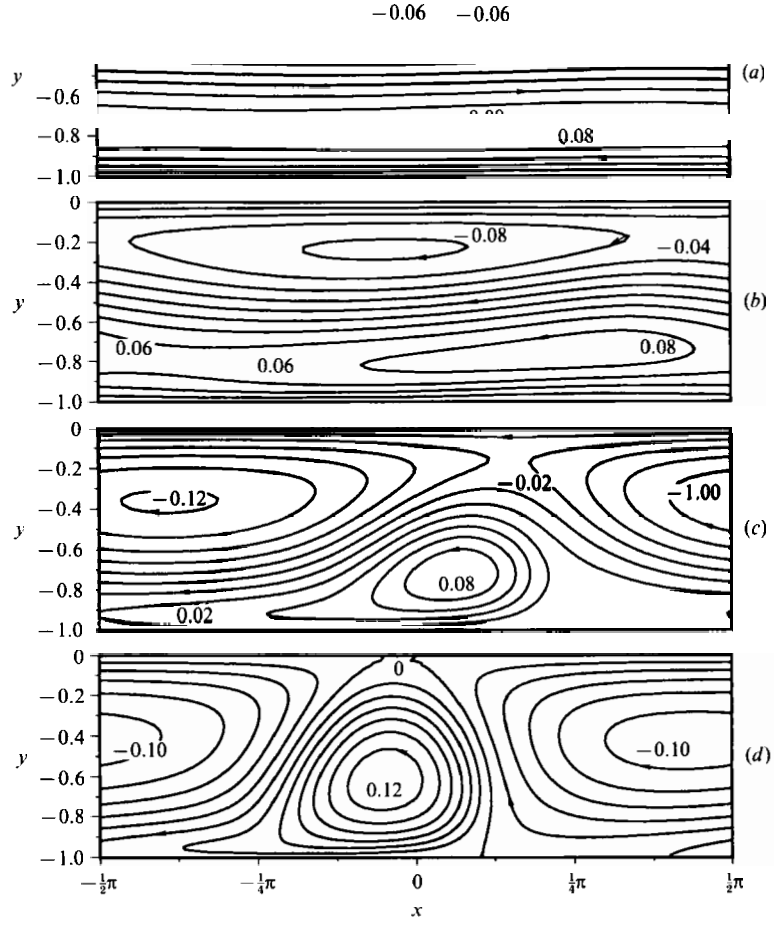

FIGURE 6. Lagrangian streamlines ($\Delta\chi = 0.02$) in partially reflected waves for $\delta = 0.04$ and (*a*) $R = 0.1$, (*b*) $R = 0.3$, (*c*) $R = 0.5$, (*d*) $R = 0.7$.

as the wave reaches the standing wave limit. The Lagrangian streamlines (particles paths) and vorticity contours, figures 6 and 7, are drawn to follow the development of the jet already mentioned in the standing wave case. The jet formation depends more on the reflection coefficient to induce a flow reversal at the seabed, than on the value of δ. The mass transport velocity at the edge of the Stokes boundary layer is given by

$$u_m = \frac{k^3}{4\beta^2 \cosh^2 kh}[5(1-|R|^2)-6|R|\sin(\xi-\xi_0)],$$

where ξ_0 is the phase of the reflection coefficient. The velocity is positive throughout the region when $|R| \leqslant R_c = \frac{1}{5}(34)^{\frac{1}{2}}-3)$. Flow reversal occurs when $|R| \geqslant R_c$ at the two ξ-locations where

$$\sin(\xi-\xi_0) = 5(1-|R|^2)/(6|R|).$$

Recirculation cells appear well before the reflection coefficient reaches the critical value. No sign of the jet is, however, perceptible until $|R| \geqslant R_c$. This is most apparent in the streamline contours when $|R| = 0.6 > R_c$. For this case, the jet does not reach

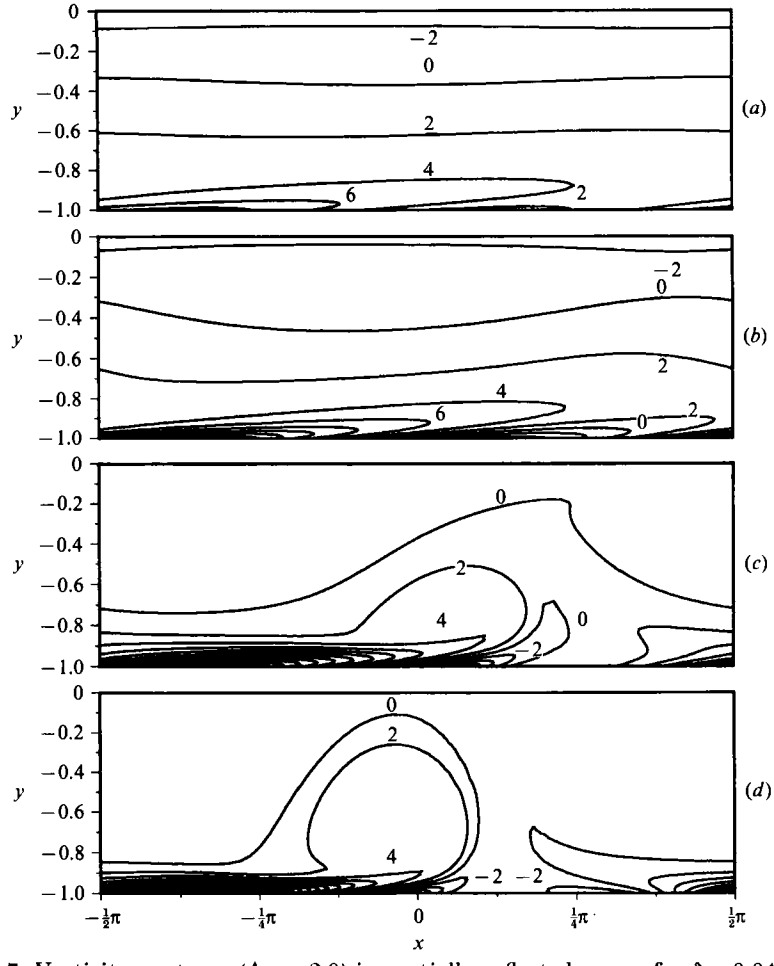

FIGURE 7. Vorticity contours ($\Delta\omega = 2.0$) in partially reflected waves for $\delta = 0.04$ and (*a*) $R = 0.1$, (*b*) $R = 0.3$, (*c*) $R = 0.5$, (*d*) $R = 0.7$.

the free surface but, rather, is deflected sideways. As $|R|$ increases, the jet axis becomes more aligned with the vertical, and the jet source moves towards the antinodal line $x = 0$.

The parameter δ bears a stronger influence on the vorticity distribution than on the velocity profiles even at small values of the reflection coefficient. Figure 8(*a–d*) compares the vertical vorticity profile along the line $x = \frac{1}{4}\pi$ for different values of $|R|$ and δ. When δ is large, the vertical vorticity distribution is almost linear and resembles the progressive wave profile; as $|R|$ approaches 1, it acquires the hyperbolic character associated with the conduction solution in standing waves (Longuet-Higgins 1953). For small δ (0.10 and 0.04), and unlike the velocity profiles in figure 4(*a–d*), the vorticity develops a boundary-layer character near the seabed even at small $|R|$-values. This is not entirely surprising as one would expect the second normal derivative of the velocity to be more singular than the first-order derivative, because each differentiation along the normal raises the order by $O(\delta^{-1})$. The large vertical vorticity gradients are confined within a distance $O(\delta)$ from the seabed. Outside this region, the vorticity gradients diminish quickly and stay at a constant value in the bulk of the flow region. One can notice an almost linear profile for the

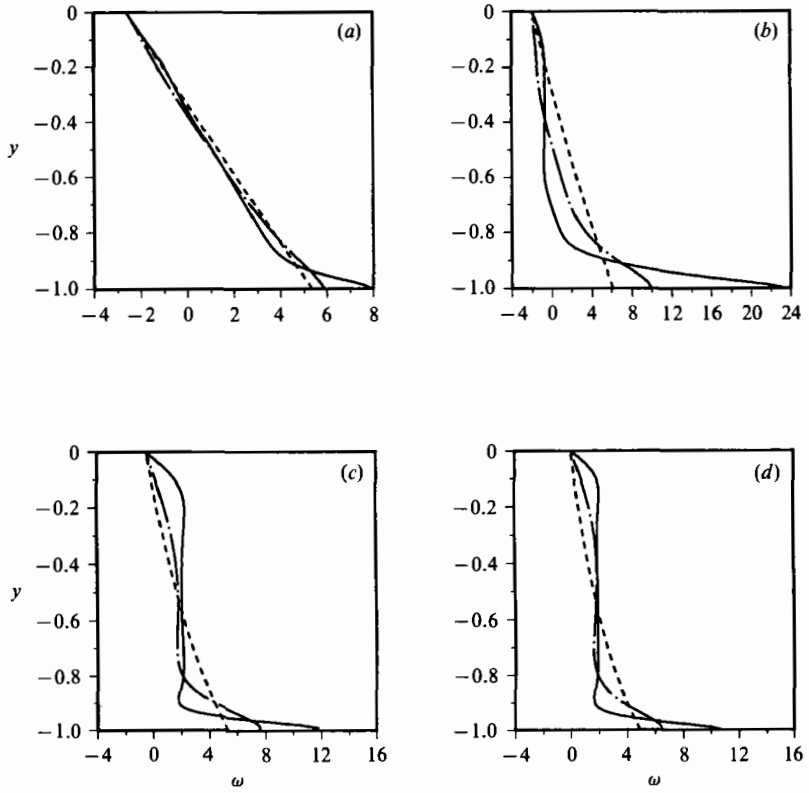

FIGURE 8. Vorticity profile at $x = -\frac{1}{4}\pi$ for δ equal to 0.04 (—), 0.1 (—·—) and 100 (– –); (*a*) $R = 0.1$, (*b*) $R = 0.5$, (*c*) $R = 0.9$, (*d*) $R = 1.0$.

vorticity when $|R|$ is small. At larger values, the vorticity becomes more uniform in the recirculation region as the streamlines become closed. A vorticity gradient is induced by the jet that forms at $|R| \geqslant 0.6$; the vorticity distribution, however, becomes more uniform on either side of the jet, as δ decreases and $|R|$ approaches 1. The vorticity contours in figure 7 for $\delta = 0.04$ support the aforementioned observations.

Spectral schemes, in contrast to other numerical methods, approximate the solution with global shape functions. This effectively restricts their applications to problems with regular geometries. Moreover, Fourier functions lose their advantages when the problem is aperiodic. In the case of water waves for example, the mass transport is not spatially periodic if the waves are propagating over uneven topography; the solution of the equations has to rely on a different formulation than the one presented in this section. Among the many numerical schemes, the FEM offers great flexibility in dealing with irregular geometry, boundary conditions and nonlinearities. Details about the FEM can be found in Baker (1983).

4. Mass transport around a localized disturbance

In this section, we investigate the mass transport around a localized disturbance in an otherwise uniform two-dimensional wave field. The disturbance is a hump located in a constant-depth region, and its size is large enough to reflect the incident wave.

The solution of the mass transport equations raises a difficult question that concerns the type of boundary conditions to apply upstream and downstream of the disturbance for, unlike the $O(\alpha)$ motion, radiation boundary conditions do not exist. These complications stem from the elliptic nature of the governing equations. If the computational domain is truncated, appropriate boundary conditions must be applied to mimic the upstream and downstream flows.

In this study, the flow domain is divided into three different regions, and the steady flow in each of them is calculated. When an incident wave encounters the disturbance, part of the wave is reflected back while the rest propagates downstream as a transmitted wave. The reflection and transmission phenomenon gives rise to local wave modes (evanescent modes) that die out quickly as one moves away from the scatterer. Far away from the scatterer, the wave field consists of a partially reflected wave upstream of the disturbance, and a purely progressive wave downstream. The mass transport is hence periodic in the upstream region and can be computed with the help of the spectral scheme, once the reflection is known. Downstream, and owing to the purely progressive nature of the transmitted wave, the mass transport is uniform in the direction of wave propagation; the solution is independent of the parameter δ and easy to compute. In the localized disturbance region, the irregular geometry imposes the recourse to the FEM scheme. The three solution domains are connected at the 'in-flow' and 'out-flow' boundaries.

In the present work, the upstream and downstream mass transport have been computed on the assumption of no net flux. The 'in-flow' and 'out-flow' terminology is, hence, not very descriptive of the present situation, for on both lateral boundaries fluid enters and leaves the computational domain. Moreover, the velocity and vorticity profiles upstream and downstream are predetermined, as the mass transport in the wave reflection and transmission regions is computed independently. It was hence deemed necessary to specify the streamline and vorticity distributions at the left and right boundary. This choice of boundary conditions entails the continuity of the horizontal component of the velocity and the normal derivative of the vertical velocity at the lateral boundaries. The question remains: how large should the computational region be to minimize the influence of the boundaries on the flow near the disturbance? Various numerical experiments were carried out to investigate this issue and, at least for the cases considered, the mass transport profiles and streamlines seemed to converge as the boundaries were farther than one wavelength away from the disturbance.

The computations of the mass transport proceeds in three steps. First the $O(\alpha)$ irrotational wave field is computed with the help of the boundary integral equation method (BIEM) (Liu & Abaspour 1982), and the forcing terms for the mass transport are evaluated. Second, the mass transport in the regions of wave reflection and transmission is computed. Third, the results from steps one and two are combined, and the equations governing the mass transport are solved numerically in the flow region containing the seabed disturbance. The computational effort increases appreciably since the first-order wave field cannot be obtained analytically.

4.1. *Hump*

The seabed profile is symmetric about $x = 0$ with the following bathymetry:

$$h(x) = \begin{cases} h_1 & (|x| \geqslant x_0) \\ (h_1 - h_2)\left[\left(\dfrac{x}{x_0}\right)^6 - 3\left(\dfrac{x}{x_0}\right)^4 + 3\left(\dfrac{x}{x_0}\right)^2\right] + h_2 & (|x| \leqslant x_0). \end{cases} \tag{35}$$

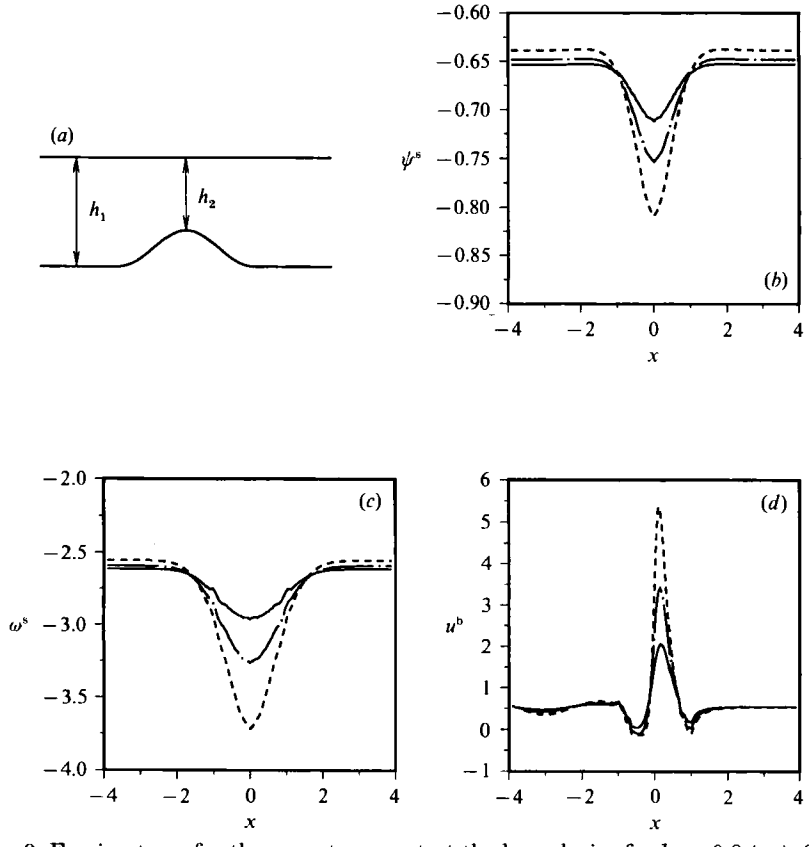

FIGURE 9. Forcing term for the mass transport at the boundaries for $h_2 = 0.8$ (—), 0.7 (—·—) and 0.6 (– –). (*a*) Geometry of the hump. (*b*) Eulerian stream function at the free surface $\psi(x, 0)$. (*c*) Vorticity at the free surface $\omega(x, 0)$. (*d*) Eulerian streaming at the seabed $u(x, -1)$.

The water depth is $h_2 \leqslant h_1$ at $x = 0$, and h_1 at $x = \pm x_0$; the geometry is sketched in figure 9(*a*). The simulation was done for $x_0 = h_1 = k = 1.0$, and the height of the hump was put successively at $h_2 = 0.6$, 0.7, and 0.8. The reflection/transmission of a progressive wave travelling from $x \sim -\infty$ over the hump was calculated by using potential flow theory and the BIEM. The solution yielded the potential for the wave field as well as the reflection and transmission coefficients. The wave exhibited little reflection in view of the mild sloping topography. The reflection coefficient had a magnitude of 0.165, 0.112 and 0.067 for h_2 equal to 0.6, 0.7, and 0.8, respectively; the transmission coefficient was equal to 0.986, 0.994, and 0.998.

Once the potential flow was known, the numerical evaluation of (7), (8) and (9) yielded the stream function ($\psi^s = \bar{\psi}_2(x, 0)$ with $\chi = 0$) and vorticity ($\omega^s = \bar{\omega}_2(x, 0)$) on the surface and the Eulerian velocity on the seabed ($u^b = \bar{u}_2(x, -h)$). The Stokes drift was calculated from (3). Iskandarani (1991) provides more details on the BIEM solution and the computations of forcing terms for the mass transport. The surface forcing terms, ψ^s and ω^s, and the Eulerian streaming at the seabed, u^b, are shown in figures 9(*b*)–9(*d*) for the case $k = 1.0$, and $h_2 = 0.8$, 0.7, and 0.6. The first two figures (9*b*, *c*) show the variations of the stream function ψ^s and vorticity ω^s at the free surface; both attain their peak at the crest of the hump. Figure 9(*d*) depicts the Eulerian velocity at the seabed; as one moves downstream, u^b decreases from a positive nearly constant value to a minimum, and then increases rapidly to reach a

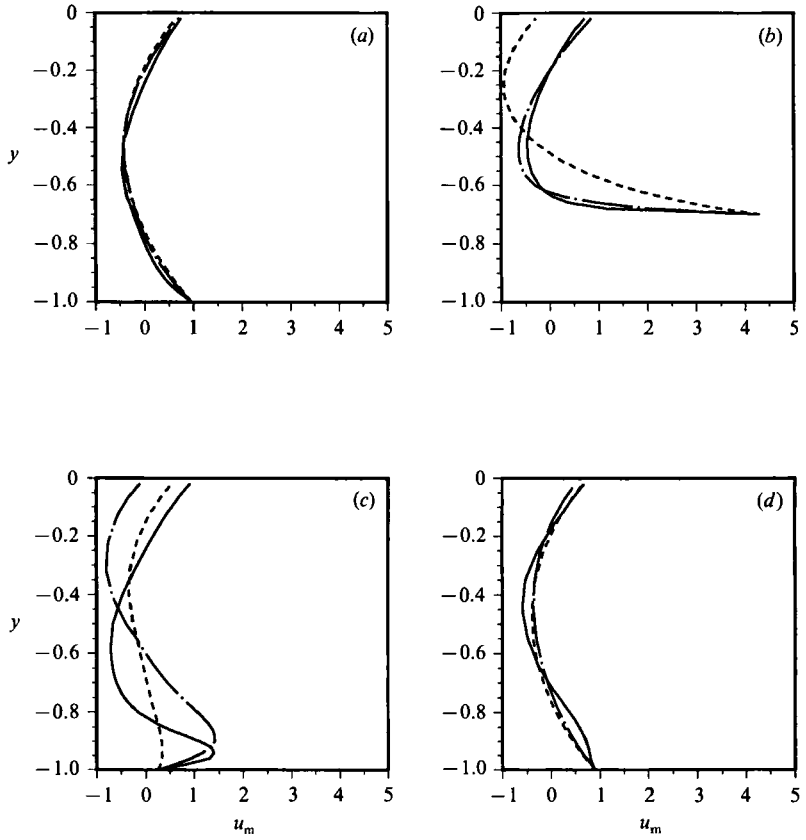

FIGURE 10. Mass transport velocity profile at different sections above a hump for $h_2 = 0.7$ and δ equal to 0.05 (—), 0.1 (—·—), 100 (--); (*a*) $x = -1.9$, (*b*) $x = 0$, (*c*) $x = 1.0$, (*d*) $x = 2.5$.

maximum value just to the right of the crest. On the lee side, u^b decreases rapidly first, then increases gradually before it levels off as one reaches the constant-water-depth region.

The spectral solution described previously was employed to calculate the mass transport in the partially reflected wave region upstream of the hump. Downstream of the hump the mass transport was uniform and was obtained analytically. The stream function and vorticity were now known on the lateral sides, and the boundary conditions for the mass transport equations were completed. Finally, the mass transport equations were solved using the FEM. The mass transport horizontal velocity profiles are shown in figure 10(*a–d*) at different sections of the flow. The different curves compare the influence of the parameter δ, for the three values 100 (conduction solution of Longuet-Higgins), 0.1 and 0.05. The formation of the so-called Stuart boundary layer at the seabed is most apparent at the hump crest ($x = 0$) in figure 10(*b*). The velocity profile exhibits larger gradients near $y \sim -h_2 + O(\delta)$, where the velocity decreases rapidly from its value at the outer edge of the Stokes layer. The slope of the velocity profile in the Stuart layer, $|\partial u_m/\partial y|$, increases as δ decreases. The mass transport is not confined to this outer boundary layer, but extends throughout the flow domain. The mass transport velocity at the free surface seems to depend crucially on δ; in certain instances the backward drift at the free surface becomes forward as the value of δ is increased or decreased. As one moves

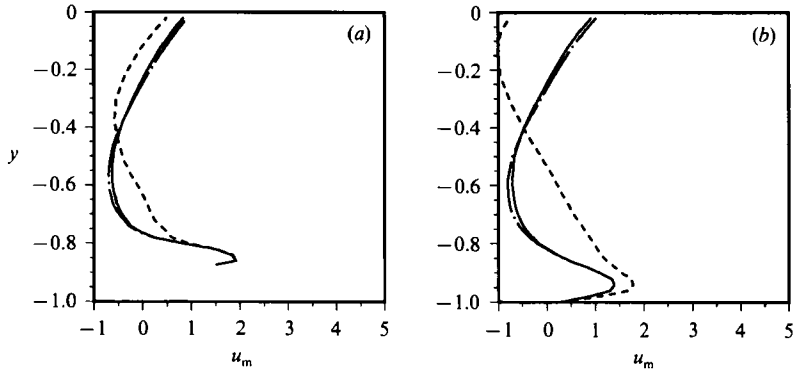

FIGURE 11. Comparison of the effects of truncating the flow domain on the mass transport velocity, $h_2 = 0.7$, Mesh 3: $|x| \leqslant 4$ (—), Mesh 2: $|x| \leqslant 3$ (—·—), Mesh 1: $|x| \leqslant 2$ (--); (*a*) $x = 0.5$, (*b*) $x = 1.0$.

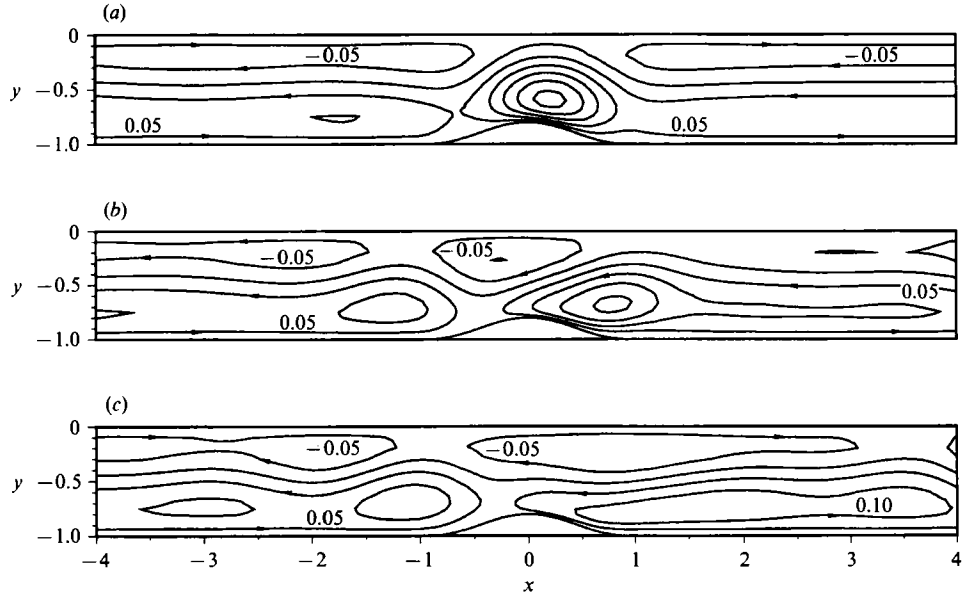

FIGURE 12. Lagrangian streamlines for $h_2 = 0.8$ and (*a*) $\delta = 100$, (*b*) $\delta = 0.10$, (*c*) $\delta = 0.05$; the streamlines increment is $\Delta\chi = 0.05$.

further downstream of the hump, the dependency of the flow on δ diminishes, and the flow acquires the profile associated with a purely progressive wave. The same holds true upstream because of the small reflection; however, smaller values of δ would accentuate the discrepancies in the three profiles. Similar velocity profiles were obtained for the other two cases considered, $h = 0.6$ and 0.8.

Three meshes with different lengths were used to test the effects of truncating the computational region. The three intervals were $|x| \leqslant 2$ (Mesh 1), $|x| \leqslant 3$ (Mesh 2) and $|x| \leqslant 4$ (Mesh 3). The velocity profiles associated with each mesh were compared for $h_2 = 0.7$ and δ equal to 100, 0.1, and 0.05 respectively. These profiles coincided at all sections for δ equal to 100, and differed slightly at sections in the lee of the disturbance for δ equal to 0.1. The differences increase as δ decreases, especially downstream of the hump. Figure 11 (*a*, *b*) depicts the case $\delta = 0.05$ at sections where the discrepancies are most dramatic. However the results of Mesh 2 and Mesh 3, in

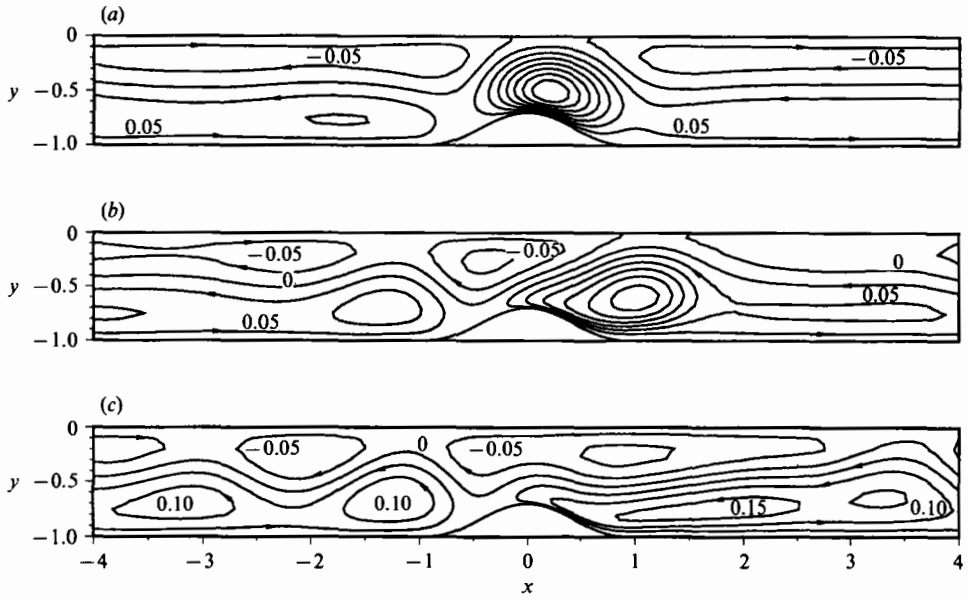

FIGURE 13. Lagrangian streamlines for $h_2 = 0.7$ and (*a*) $\delta = 100$, (*b*) $\delta = 0.10$, (*c*) $\delta = 0.05$; streamlines increment $\Delta\chi = 0.05$.

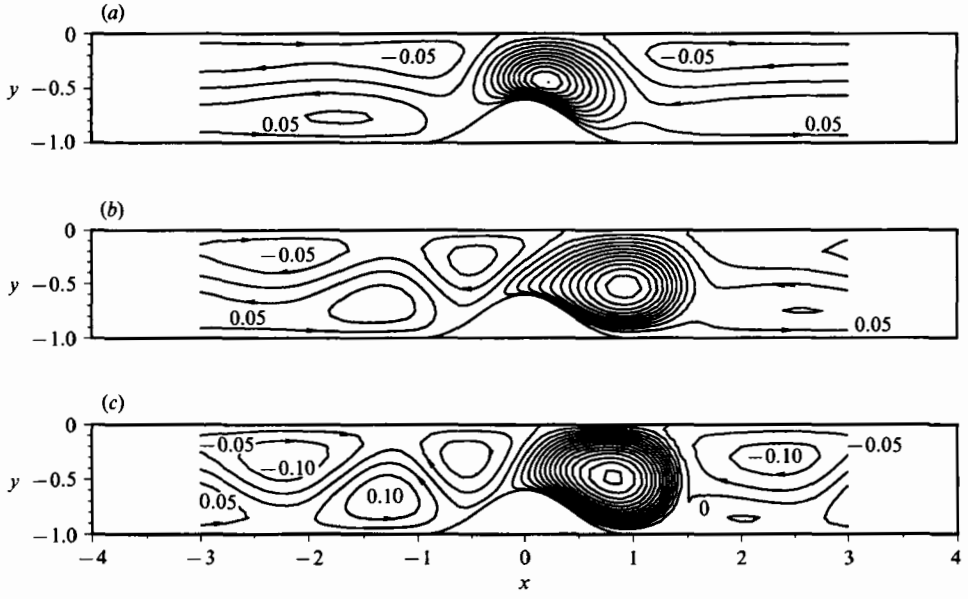

FIGURE 14. Lagrangian streamlines for $h_2 = 0.6$ and (*a*) $\delta = 100$, (*b*) $\delta = 0.10$, (*c*) $\delta = 0.05$; streamlines increment $\Delta\chi = 0.05$.

contrast to the Mesh 1 profiles, are in reasonable agreement and give us some confidence in the numerical solution. The end effect will always be present because of the Dirichlet boundary conditions. The flow inside the computational region does not contribute to the boundary distributions of the streamlines and vorticity. Instead it is forced to accommodate the imposed boundary conditions. The flow features next to the lateral boundaries will keep shifting as the lateral sides are moved further away from the scatterer. When the lateral boundaries are far enough,

their location does not seem to affect the flow near the hump. Figures 12–14 show the Lagrangian streamlines (path lines) for different h_2. One can see the formation of a recirculating region on the lee side of the hump. It decreases in size, in figures 12 and 13, as δ is decreased. In figure 14 on the other hand, the size of the recirculating region seems to increase for smaller δ, and when $\delta = 0.05$ its size prevents the fluid from crossing over the hump.

5. Conclusions

A Fourier–Chebyshev spectral method has been presented for the solution of mass transport equations when the steady flow is periodic. The no-slip boundary condition on the velocity at the seabed has been recast into an integral equation on the vorticity coefficients of each Fourier mode. The spectral scheme is adopted to investigate mass transport over a uniform depth in partially reflected waves. The development of the so-called double boundary layer depends on the smallness of the parameter δ, and on the gradients of the Reynolds stresses (the Stokes drift) which, in turn, are a function of the reflection coefficient. As reflection increases, these gradients become directly involved in the convection and generation of the mean flow (Riley 1984). The contour lines reveal the formation of recirculating cells where the vorticity is uniformly distributed.

The spectral scheme was also used in the study of a wave propagating over an isolated disturbance in the topography. An FEM scheme was employed to solve the governing equations in the neighbourhood of the hump. Numerical investigations revealed the formation of a large recirculating cell on the lee side. The size and magnitude of this circulation depended on δ, and the geometry of the hump. The main part of this work hinges on the 'in-flow' and 'out-flow' boundary conditions. Since radiation boundary conditions for the mean flow are lacking, assumptions have to be made regarding the nature of the flow away from the scatterer. These assumptions are reflected in the type of boundary conditions applied at the lateral sides of the computational domain.

The present investigations have been limited to two-dimensional flows where the vortex stretching vanishes. Results on mass transport in the interior region of three-dimensional waves are the subject of another paper (Iskandarani & Liu 1991). If the first-order motion consists of a short-crested wave, the mass transport can be shown to be periodic in two horizontal directions. Fourier series can again be used to develop a numerical scheme similar to the one presented here. The formulation can be either extended through the use of a three-dimensional streamfunction (a vector potential) or recast into a velocity–vorticity formulation.

The research was supported by a grant from the National Science Foundation (CTS-8902407). Computer facilities and funds were provided by the Cornell National Supercomputer Facility (CNSF).

Appendix

When $n = 0$,

$$S_{m,0} = \begin{cases} S_{m,0} = \dfrac{2}{m^2-1} & \text{if } m \text{ is even} \\ S_{m,0} = \dfrac{-2}{m^2-4} & \text{if } m \text{ is odd;} \end{cases} \tag{A 1}$$

when $n \neq 0$,
$$S_{m,n} = \sum_{p=0}^{\infty} b_{m,p} a_{p,n}, \tag{A 2}$$

where

$$A_{p,n} = \begin{cases} \dfrac{-I_p(nkh)}{c_p \cosh nkh} & \text{if } p \text{ is even} \\ \dfrac{I_p(nkh)}{c_p \sinh nkh} & \text{if } p \text{ is odd,} \end{cases} \tag{A 3}$$

$$b_{m,p} = \begin{cases} \dfrac{-2(m^2+p^2-1)}{[(m+p)^2-1][(m-p)^2-1)]} & \text{if } (m+p) \text{ even} \\ 0 & \text{if } (m+p) \text{ odd.} \end{cases} \tag{A 4}$$

I_p refers to the modified Bessel function of the first kind and order p.

REFERENCES

BAKER, A. J. 1983 *Finite Element Computational Fluid Mechanics.* Hemisphere.

BATCHELOR, G. K. 1967 *An Introduction to Fluid Dynamics.* Cambridge University Press.

BERTELSEN, A., SVARDAL, A. & TJØTTA, S. 1973 Nonlinear streaming effects associated with oscillating cylinders. *J. Fluid Mech.* **59**, 493–511.

BOYD, J. P. 1989 *Chebyshev and Fourier Spectral Methods* (ed. C. A. Brebbia & S. A. Orszag), Lecture Notes in Engineering. Springer.

CANUTO, C., HUSSAINI, M. Y., QUARTERONI, A. & ZANG, T. A. 1988 *Spectral Methods in Fluid Dynamics. Springer Series in Computational Physics.* Springer.

DORE, B. D. 1976 Double boundary layer in standing surface waves. *Pure Appl. Geophys.* **114**, 629–637.

DUCK, P. W. & SMITH, F. T. 1979 Steady streaming induced between oscillating cylinders. *J. Fluid Mech.* **91**, 93–110.

GOTTLIEB, D. & ORSZAG, S. A. 1977 *Numerical Analysis of Spectral Methods: Theory and Applications.* Philadelphia: SIAM-CBMS.

HADDON, E. W. & RILEY, N. 1983 A note on the mean circulation in standing waves. *Wave Motion* **5**, 43–48.

ISKANDARANI, M. 1991 Mass transport in two- and three-dimensional water waves. PhD thesis, Cornell University.

ISKANDARANI, M. & LIU, P. L.-F. 1991 Mass transport in three-dimensional water waves. *J. Fluid Mech.* **231**, 417–437.

LIU, P. L.-F. & ABBASPOUR, M. 1982 An integral equation method for the diffraction of oblique waves by an infinite cylinder. *Intl J. Numer. Method. Engng* **18**, 1497–1504.

LONGUET-HIGGINS, M. S. 1953 Mass transport in water waves. *Phil. Trans. R. Soc. Lond.* A **245**, 535–581.

LONGUET-HIGGINS, M. S. 1960 Mass transport in the boundary layer at a free oscillating surface. *J. Fluid Mech.* **8**, 293–306.

RILEY, N. 1965 Oscillating viscous flows. *Mathematika* **12**, 161–175.

RILEY, N. 1984 Progressing surface waves on a liquid of non-uniform depth. *Wave Motion* **6**, 15–22.

ROACHE, P. J. 1982 *Computational Fluid Dynamics.* Hermosa.

RUSSELL, R. C. H. & OSORIO, J. D. C. 1958 An experimental investigation of drift profiles in a closed channel. In *Proc. Sixth Conf. on Coastal Engng*, pp. 171–193. ASCE.

STUART, J. T. 1966 Double boundary layer in oscillatory viscous flow. *J. Fluid Mech.* **24**, 673–687.

ÜNLÜATA, Ü. & MEI, C. C. 1970 Mass transport in water waves. *J. Geophys. Res.* **75**, 7611–7618.